Efficient multipole representation for matter-wave optics

J. Teske ⓘD ; R. Walser ⓘD

Check for updates

View Online

Export Citation

CrossMark

AVS Quantum Science

AVS

AIP Publishing

Efficient multipole representation for matter-wave optics

View Online   Export Citation   CrossMark

J. Teske[a] 🔵 and R. Walser 🔵

AFFILIATIONS

Technical University of Darmstadt, Institute of Applied Physics, Darmstadt, Germany

Note: This paper is part of the Large Scale Quantum Detectors Special Issue.
[a]Electronic mail: jan.teske@physik.tu-darmstadt.de

ABSTRACT

Technical optics with matter waves requires a universal description of three-dimensional traps, lenses, and complex matter-wave fields. In analogy to the two-dimensional Zernike expansion in beam optics, we present a three-dimensional multipole expansion for Bose-condensed matter waves and optical devices. We characterize real magnetic chip traps, optical dipole traps, and the complex matter-wave field in terms of spherical harmonics and radial Stringari polynomials. We illustrate this procedure for typical harmonic model potentials as well as real magnetic and optical dipole traps. Eventually, we use the multipole expansion to characterize the aberrations of a ballistically interacting expanding Bose–Einstein condensate in $(3+1)$ dimensions. In particular, we find deviations from the quadratic phase ansatz in the popular scaling approximation. The scheme is data efficient by representing millions of complex amplitudes of a field on a Cartesian grid in terms of a low order multipole expansion without precision loss. This universal multipole description of aberrations can be used to optimize matter-wave optics setups, for example, in matter-wave interferometers.

I. INTRODUCTION

In 1934, Frits Zernike introduced the orthogonal "Kreisflächenpolynome" to describe the optical path difference between light waves and a spherical reference wavefront.[1] Understanding the phase differences and minimizing the optical aberrations laid the base for the first phase-contrast microscope.[2] This invention was awarded with the Nobel Prize in Physics in 1953. Nowadays, Zernike polynomials are widely used in optical system design as a standard description of imperfections in optical imaging.[3] Typical wavefront errors are known as defocus, astigmatism, coma, spherical aberration, etc.[4] Balancing aberrations is also relevant for optical imaging with electron microscopes.[5–8] In contrast to visible light, massive particles, such as electrons, atoms, and even larger molecules,[9] have a much smaller de Broglie wavelength, $\lambda_{dB} = h/p$, and therefore a higher resolution.

Nowadays, atom-interferometers with ultracold atoms are used to study fundamental scientific questions like tests of the Einstein equivalence principle,[10–12] probing the quantum superposition on macroscopic scales,[13] the search for dark matter candidates[14] and gravitational waves.[15,16] Kip Thorne's multipole representation of weak gravitational waves[17] was a major step stone toward the discovery[18]

and the efficient data analysis. Being very sensitive to accelerations and rotations, atom interferometry could be used for inertial sensing, replacing commercial laser gyroscopes, and satellite navigation in space.[19] Common to all μg-interferometric measurements with Bose–Einstein condensates are long expansion times[20] to reduce mean-field interaction as well as to increase the sensitivity of the interferometer. Hence, it is crucial to understand the actual shape of the condensate's phase as it determines the interference patterns at the end of the interferometer.[21–23]

Inspired by Zernike's work, we will adopt his approach to analyze these aberrations in the world of matter waves:

First, we introduce a multipole expansion with suitable polynomial basis functions in Sec. II. We consider spherical-, spheroidal-, displaced asymmetric harmonic-, and generally asymmetric trapping potentials in Sec. III. In particular, we characterize the magnetic potential from a realistic atom chip model. In Sec. IV, we extend the multipole analysis to Bose–Einstein condensates in the strongly interacting Thomas–Fermi as well as in the low interacting limit. Finally, we investigate the shape of the phase profile for a ballistically expanding condensate in Sec. V and discuss the efficiency of our multipole expansion in Sec. VI.

04 March 2024 12:38:33

II. MULTIPOLE EXPANSION WITH STRINGARI POLYNOMIALS

A. Orthogonal function within a sphere

Cold atoms can be trapped or guided in either optical dipole or Zeeman potentials.[24] If these potentials are applied for short times (impact approximation, phase imprinting[25]), one modifies only the phase of the atomic wave packet, thus, the momentum distribution of the condensate. This process is equivalent to a *thin lens* in optics, but now in $(3+1)$ dimensions.[26] Systematically analyzing the features of different potentials becomes crucial for achieving the ultimate precision in long-time atom interferometry.[27]

The standard Taylor expansion of a potential, in the vicinity of a point r_0, reads in three-dimensional Cartesian coordinates $r = r_0 + \zeta$,

$$U(r) = U_0 + \zeta^\top \nabla U_{|r_0} + \frac{1}{2} \zeta^\top \mathsf{K} \zeta + \cdots . \qquad (1)$$

This interpolation polynomial is useful for extracting forces from the gradient or trapping frequencies from the eigenvalues of the Hesse matrix $\mathsf{K} = (\nabla \otimes \nabla U)_{|r_0}$. However, the Taylor series are notoriously inefficient approximation schemes.

Alternatively, we introduce a multipole expansion in spherical coordinates (r, ϑ, φ),

$$\langle r|U \rangle = U(r) = \sum_{n=0}^{\infty} \sum_{l=0}^{\infty} \sum_{m=-l}^{l} U_{nlm} \langle r|nlm \rangle, \qquad (2)$$

in terms of multipole coefficients, $U_{nlm} = \langle nlm|U \rangle$, and orthonormal basis functions,

$$\langle r|nlm \rangle = S_{nlm}(r) = S_{nl}(r) Y_{lm}(\vartheta, \varphi), \qquad (3)$$

$$\langle n'l'm'|nlm \rangle = \delta_{n,n'} \delta_{l,l'} \delta_{m,m'}, \qquad (4)$$

consisting of spherical harmonics $Y_{lm}(\vartheta, \varphi)$ and radial polynomials $S_{nl}(r)$. Explicitly, they have support within a hard three-dimensional "aperture" of radius R. In terms of a scaled aperture radius $0 \leq \tilde{r} = r/R \leq 1$, they read

$$S_{nl}(r) = \mathcal{N}_{nl} \tilde{r}^l J_n^{(l+1/2, 0)}(1 - 2\tilde{r}^2), \qquad (5)$$

where $J_n^{(l+1/2,0)}$ denotes the Jacobi polynomials[28] (see Appendix A). The polynomials in Eq. (5) describe the sound wave excitations of a Bose–Einstein condensate in the strong interacting Thomas–Fermi limit for an isotropic three-dimensional harmonic oscillator potential, originally described by Stringari[29] and Öhberg et al.[30] Thus, these fundamental modes are well adapted for condensates in harmonic as well as in more realistic trapping geometries (see Secs. III C and V). In hindsight, it almost seems natural to recover Jacobi polynomials $J_n^{(l+1/2,0)}$ with half-integral indices in the three-dimensional situation, if we compare this to the circle polynomials of Zernike in two-dimensional beam optics.[31] The normalization $\mathcal{N}_{nl} = [(4n + 2l + 3)/R^3]^{1/2}$ renders the polynomials orthonormal on the interval $0 \leq r \leq R$,

$$\int_0^R dr \, r^2 S_{n'l}(r) S_{nl}(r) = \delta_{n,n'}. \qquad (6)$$

Therefore, the potential expansion coefficients U_{nlm} in Eq. (2) are given by the overlap integral

$$U_{nlm} = \langle nlm|U \rangle = \int_V d^3 r \, S_{nlm}^*(r) U(r), \qquad (7)$$

within a spherical volume $V = 4\pi R^3/3$. Typically, the characteristic size of the wave packet in the trap determines the aperture radius R. For cold clouds, this size is of the order of the harmonic oscillator length $\ell = \sqrt{\hbar/(M\omega)}$ for a non-interacting gas or for an interacting condensate, the Thomas–Fermi radius $r_{\mathrm{TF}} = \sqrt{2\mu/(M\omega^2)}$. For thermal clouds, the radius $R \approx \sqrt{k_B T/(M\omega^2)}$ is proportional to the temperature T.

Instead of a multipole expansion of the potential in Eq. (36), it is also possible to decompose the logarithm of the potential,

$$\theta(r) = -\log \frac{U(r)}{U_0} = \sum_{n=0}^{\infty} \sum_{l=0}^{\infty} \sum_{m=-l}^{l} \theta_{nlm} \langle r|nlm \rangle. \qquad (8)$$

This cumulant expansion[32] is particularly useful for Gaussian functions as the series terminates quickly after the second order. In Sec. III, we analyze both the potentials and their cumulants in terms of these multipole expansions.

B. Spectral powers

For interpreting and visualizing the complex expansion coefficient U_{nlm} or θ_{nlm}, we introduce relative spectral powers, $p_{nl} \geq 0$. The latter is independent of the potential's orientation to the reference coordinate system. This also holds for the cumulant expansion in Eq. (8). Let us consider a coordinate transformation $r' = \mathsf{R}r$, where R denotes an orthogonal rotation matrix $\mathsf{RR}^\top = \mathbb{1}$. In both frames, the values of the potential agree,

$$\langle r|U \rangle = \langle r'|U' \rangle = \sum_{nlm'} \langle r'|nlm' \rangle U'_{nlm'}. \qquad (9)$$

The coefficients in the new reference frame U'_{nlm} are given by

$$U'_{nlm'} = \sum_{m=-l}^{l} D_{m'm}^{(l)}(\mathsf{R}) U_{nlm}, \qquad (10)$$

where the $D_{m'm}^{(l)}(\mathsf{R}) = \langle lm'|\hat{R}|lm \rangle$ are the Wigner D-matrices as the matrix representation of the rotation operator $\hat{R}$ in the angular momentum basis.[33–35] Using the unitarity of the rotation operator, $\hat{R}\hat{R}^\dagger = \hat{R}^\dagger \hat{R} = \mathbb{1}$, as well the orthonormality of the Stringari polynomials (3), we specify rotational invariant measures such as the total power,

$$P(U) = \int_V d^3 r \, |U(r)|^2 = \sum_{nlm} |U_{nlm}|^2. \qquad (11)$$

Moreover, we define the marginals P_{nl} and P_l,

$$P_{nl}(U) = \sum_{m=-l}^{l} |U_{nlm}|^2, \quad P_l(U) = \sum_n P_{nl}(U), \qquad (12)$$

as well as the relative fractional powers $p_{nl}(U)$ by

$$p_{nl}(U) = \frac{P_{nl}(U)}{P(U)} \quad \sum_{nl} p_{nl}(U) = 1. \qquad (13)$$

Thus, the relative fractional powers add up to one.

III. MULTIPOLE EXPANSION OF TRAPS
A. Harmonic, isotropic, three-dimensional oscillator

A stiffness parameter k characterizes a harmonic, isotropic, three-dimensional oscillator potential,

$$U(\boldsymbol{r}) = \frac{k}{2}r^2 = \sum_{n=0}^{1} U_{n00}\langle \boldsymbol{r}|n00\rangle = \frac{3}{5}u\langle\boldsymbol{r}|000\rangle - \sqrt{\frac{12}{175}}u\langle\boldsymbol{r}|100\rangle. \tag{14}$$

For a particle with mass M, the angular frequency $\omega = \sqrt{k/M}$. An isotropic potential is invariant under rotations. Thus, only the s-waves contribute. A Stringari polynomial S_{n0} from Eq. (5) is of the order r^{2n}, which limits the radial modes to two monopoles. The expansion coefficients U_{n00} are given in terms of a dimensional factor ($Jm^{3/2}$),

$$u = \frac{k}{2}R^2\sqrt{V}. \tag{15}$$

For the total power, one finds

$$P(U) = \frac{3}{7}u^2, \tag{16}$$

as well as the fractional powers,

$$p_{00}(U) = \frac{21}{25} = 0.84, \quad p_{10}(U) = \frac{4}{25} = 0.16. \tag{17}$$

B. Harmonic, anisotropic, three-dimensional oscillator
1. Spheroidal potential

For a prolate or oblate spheroidal harmonic oscillator, the potential is characterized by two stiffness constants $k_\perp$ and $k_\parallel$, but it is still rotational symmetric around the z-axis,

$$U(\boldsymbol{r}) = \frac{k_\perp}{2}(x^2 + y^2 + \alpha^2 z^2). \tag{18}$$

The anisotropy is measured by $\alpha^2 = k_\parallel/k_\perp$. In contrast to the isotropic oscillator, one needs also a quadrupole within the multipole expansion,

$$U_{000} = \frac{2+\alpha^2}{5}u, \quad U_{100} = -\frac{4+2\alpha^2}{\sqrt{525}}u,$$
$$U_{020} = -\frac{2-2\alpha^2}{\sqrt{105}}u, \quad u = \frac{k_\perp}{2}R^2\sqrt{V}. \tag{19}$$

Using the coefficients in Eq. (19), we can evaluate the total power

$$P(U) = \frac{8+4\alpha^2+3\alpha^4}{35}u^2 \tag{20}$$

and the relative fractional powers

$$p_{00}(U) = \frac{7}{5}\frac{(2+\alpha^2)^2}{8+4\alpha^2+3\alpha^4},$$
$$p_{10}(U) = \frac{4}{15}\frac{(2+\alpha^2)^2}{8+4\alpha^2+3\alpha^4}, \tag{21}$$
$$p_{02}(U) = \frac{4}{3}\frac{1-\alpha^2}{8+4\alpha^2+3\alpha^4}$$

for the cylindrical symmetric oscillator potential. It is noteworthy that this expansion encompasses degenerate traps with vanishing z-confinement $\alpha = 0$ as well as isotropic traps with $\alpha = 1$ from Eq. (17).

2. Tilted, shifted anisotropic harmonic oscillator potential

We consider a general harmonic oscillator potential with a symmetric stiffness matrix K localized at a position $\boldsymbol{r}_0$,

$$U(\boldsymbol{r}, \boldsymbol{r}_0) = (\boldsymbol{r} - \boldsymbol{r}_0)^\top \frac{\mathsf{K}}{2}(\boldsymbol{r} - \boldsymbol{r}_0)$$
$$= \boldsymbol{r}_0^\top \frac{\mathsf{K}}{2}\boldsymbol{r}_0 - \boldsymbol{r}_0^\top \mathsf{K}\boldsymbol{r} + \boldsymbol{r}^\top \frac{\mathsf{K}}{2}\boldsymbol{r}$$
$$= U^{(0)}(\boldsymbol{r}_0) + U^{(1)}(\boldsymbol{r}, \boldsymbol{r}_0) + U^{(2)}(\boldsymbol{r}), \tag{22}$$

and gather it into homogeneous potentials $U^{(n)}(\boldsymbol{r})$ of degree n. In order to determine the multipole expansion, we transform the position vectors $\boldsymbol{r} = x\boldsymbol{e}_x + y\boldsymbol{e}_y + z\boldsymbol{e}_z$ given in a Cartesian basis $\{\boldsymbol{e}_x, \boldsymbol{e}_y, \boldsymbol{e}_z\}$ to the spherical basis $\{\boldsymbol{e}_1, \boldsymbol{e}_0, \boldsymbol{e}_{-1}\}$,

$$\boldsymbol{e}_1 = -\frac{\boldsymbol{e}_x + i\boldsymbol{e}_y}{\sqrt{2}}, \quad \boldsymbol{e}_0 = \boldsymbol{e}_z, \quad \boldsymbol{e}_{-1} = \frac{\boldsymbol{e}_x - i\boldsymbol{e}_y}{\sqrt{2}}, \tag{23}$$

which are orthogonal with respect to the standard complex scalar-product $\boldsymbol{e}_n \boldsymbol{e}_m^* = \delta_{n,m}$. It is convenient to introduce also a dual basis $\{\boldsymbol{e}^1, \boldsymbol{e}^0, \boldsymbol{e}^{-1}\}$ with

$$\boldsymbol{e}^m = (-1)^m \boldsymbol{e}_{-m} = \boldsymbol{e}_m^*, \tag{24}$$
$$\boldsymbol{e}_n \boldsymbol{e}^m = \boldsymbol{e}_n \boldsymbol{e}_m^* = \delta_{n,m}. \tag{25}$$

Now, the position vector in the co- and contravariant spherical basis[33] reads

$$\boldsymbol{r} = \sum_{m=-1}^{1} q^m \boldsymbol{e}_m = \sum_{m=-1}^{1} q_m \boldsymbol{e}^m, \tag{26}$$
$$q_{\pm 1} = \mp \frac{x \pm iy}{\sqrt{2}}, \quad q_0 = z. \tag{27}$$

More generally, one can express the spherical vector components[36] q_m by

$$q_m = \left(\frac{4\pi}{3}\right)^{1/2} Y_{1m}(\vartheta, \varphi)r = T_m^{(1)}(\vartheta, \varphi)r, \tag{28}$$

with the spherical tensor $T_m^{(1)}(\vartheta, \varphi)$.

Obviously, the constant $U^{(0)}(\boldsymbol{r}_0) = \boldsymbol{r}_0^\top \mathsf{K}\boldsymbol{r}_0/2$. The dipole coefficients for $U^{(1)}(\boldsymbol{r}, \boldsymbol{r}_0)$ in Eq. (22) are then given by the spherical components of the vector $\boldsymbol{r}_0$,

$$U^{(1)}(\boldsymbol{r}, \boldsymbol{r}_0) = r \sum_{m=-1}^{1} U_{1m}^{(1)}(\boldsymbol{r}_0) T_m^{(1)}(\hat{r}), \tag{29}$$
$$U_{1m}^{(1)}(\boldsymbol{r}_0) = -\sum_{s=-1}^{1} q_{0,s}^* \mathsf{K}_{ms}. \tag{30}$$

The second order contribution $U^{(2)}(\boldsymbol{r})$ in Eq. (22) contains a product of two spherical tensors that can be simplified using the Clebsch–Gordan expansion,[36]

$$T_{m_1}^{(l_1)}(\hat{r})T_{m_2}^{(l_2)}(\hat{r}) = \sum_{l=|l_1-l_2|}^{l_1+l_2} \sum_{m=-l}^{l} C_{m_1 m_2 m}^{l_1 l_2 l} T_m^{(l)}(\hat{r}), \qquad (31)$$

with Clebsch–Gordan coefficients[35] $C_{m_1 m_2 m}^{l_1 l_2 l} = \langle l_1 m_1 l_2 m_2 | lm \rangle$. Hence, we can rewrite $U^{(2)}(\boldsymbol{r})$ as

$$U^{(2)}(\boldsymbol{r}) = \frac{r^2}{2} \sum_{l=0}^{2} \sum_{m=-2}^{2} U_{lm}^{(2)} T_m^{(l)}(\hat{r}), \qquad (32)$$

$$U_{lm}^{(2)} = \sum_{r,s=-1}^{1} (-1)^s C_{r(-s)m}^{11l} \mathsf{K}_{rs}, \qquad (33)$$

with multipole coefficients that contain the matrix elements of K in the spherical basis and Clebsch–Gordan coefficients. For the radial part, one can use the results from the expansion of isotropic oscillator III A in terms of the s-wave Stringari polynomials. The total power in Eq. (11) of $U^{(2)}$ evaluates to

$$P(U^{(2)}) = 9 \frac{2\mathrm{Tr}[\mathsf{K}^2] + \mathrm{Tr}[\mathsf{K}]^2}{35\mathrm{Tr}[\mathsf{K}]^2} u^2, \quad u = \frac{\mathrm{Tr}[\mathsf{K}]}{6} R^2 \sqrt{V}. \qquad (34)$$

For an isotropic stiffness $\mathsf{K} = k\mathbb{1}$, Eq. (34) reduces to the result of the isotropic harmonic oscillator in Eq. (16).

C. Magnetic Zeeman potential of an atom chip

Magnetizable atoms can be trapped in a static magnetic field,[37]

$$U_Z(\boldsymbol{r}) = \mu_B m_F g_F |\boldsymbol{B}(\boldsymbol{r})|. \qquad (35)$$

Here, μ_B denotes the Bohr magneton, g_F the Landé factor, m_F the magnetic quantum number of the total angular momentum, and $\boldsymbol{B}(\boldsymbol{r})$ the magnetic induction field. In this work, we analyze the Zeeman potential in Eq. (35) obtained by a real-world model of a magnetic chip trap.[38] These have become popular when a miniaturization of the experimental setup is required, for example, at drop towers[39,40] and in space.[41,42] The atom chip and its functionalities are described in detail in Ref. 43. In Appendix B, we present a realistic finite-wire model of the microtrap from which we deduce the magnetic induction field [see Eq. (B2)]. Here, we consider ^{87}Rb atoms in the magnetic hyperfine state $|F=2, m_F=2\rangle$ with $g_F = 1/2$ with the set of currents as presented in Table I. The corresponding Zeeman potential, evaluated in the chip coordinate system, is depicted in Fig. 1.

For an efficient representation of the three-dimensional Zeeman potential, we use the multipole expansion in Eq. (2). For a comparison, we extract also the multipoles of the cumulant as discussed in Eq. (8). As we represent the potential on discrete lattice points, we use a least-square optimization (see Appendix C) to calculate the expansion coefficients U_{nlm} and θ_{nlm}, respectively. The results of the multipole expansion are summarized in Fig. 2. There, we show the relative fractional angular powers p_{nl} for the harmonic approximation $p_{nl}(U_{ho})$ (a), the full Zeeman potential $p_{nl}(U_Z)$ (b), and the cumulant $p_{nl}(\theta)$ (c). In each subfigure, we have used the same number of basis functions with maximal principle and angular momentum quantum numbers $n_{\max} = 3$, $l_{\max} = 5$. Moreover, the multipole expansion is performed at the position of the trap minimum, shifting the position vector in Eq. (22) by $\boldsymbol{r} = \boldsymbol{r}' + \boldsymbol{r}_0$. The latter implies a vanishing dipole component $U^{(1)}(\boldsymbol{r}, \boldsymbol{r}_0) = 0$ for the harmonic approximation.

As discussed in Sec. III B, the anisotropic harmonic oscillator potential exhibits just two monopoles and one quadrupole contribution, depicted in Fig. 2(a). For a real Z-wire trap on the atom chip, the Zeeman potential exhibits all multipoles: in particular, the monopoles p_{00}, p_{10}, dipoles with p_{01}, p_{11}, a quadrupole p_{02}, as well as the octupole with p_{03}, which is depicted in Fig. 2(b). From the dipole coefficients, we deduce that in the anharmonic trap, the position of the trap minimum does not coincide with the center-of-mass position of the trap. Thus, the application of a Zeeman lens-potential causes a finite momentum-kick to the atomic density distribution. While the dipoles affect the center of mass motion, the additional octupole causes density distortions in long-time matter-wave optics and interferometry.

Finally, we note that multipoles of higher order $l > 3$ are decreasing rapidly for our trap configuration. Comparing the direct multipole expansion to the cumulant expansion, one finds that the expansion of the cumulant series converges more slowly due to the logarithmic character of Eq. (8), see Fig. 2(c).

D. Optical dipole potential from Laguerre–Gaussian beams

In addition to magnetic trapping, atoms can be also trapped by an optical dipole potential,[44,45]

$$U_D(\boldsymbol{r}) = U_0 e^{-\theta(\boldsymbol{r})}, \quad U_0 = \hbar|\Omega_0|^2/(4\Delta), \qquad (36)$$
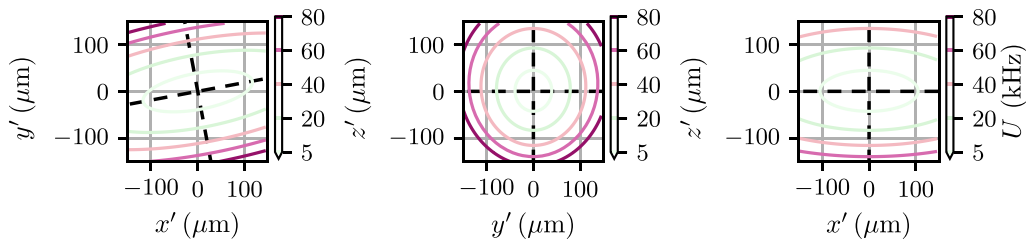

FIG. 1. Magnetic Zeeman potential of an atomic chip trap for ^{87}Rb in the magnetic substate $|F=2, m_F=2\rangle$. Two-dimensional contour plots along all three spatial planes at position $\boldsymbol{r}' = \boldsymbol{r} - \boldsymbol{r}_0$. The principle axis of the trap obtained by the Hesse matrix K Eq. (1) marked as dashed lines. Parameters of the trap are summarized in Tables I and II.
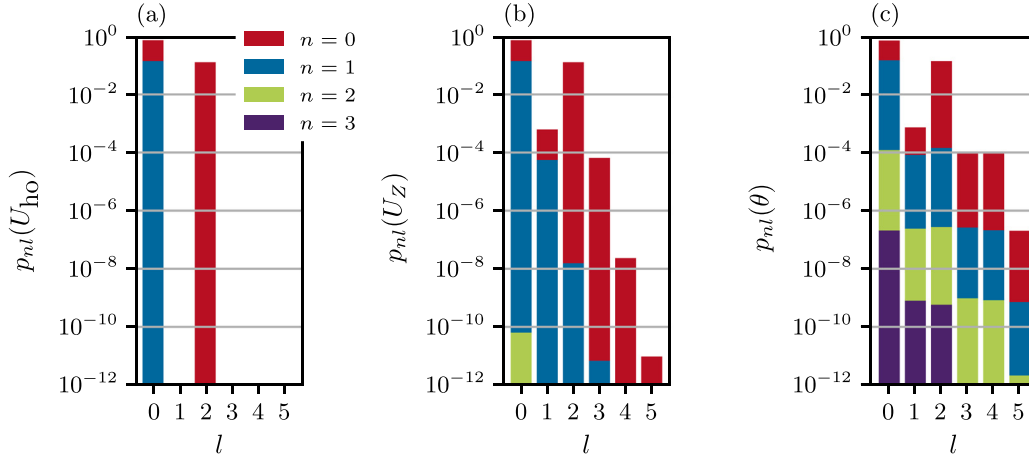
04 March 2024 12:38:33

Fɪɢ. 2. Multipole expansion of the magnetic chip trap potential. Relative powers $p_{nl}(U)$ vs angular momentum l of the Zeeman potential shown in Fig. 1. Different principle numbers: red $n = 0$, blue $n = 1$, green $n = 2$, and purple $n = 3$. (a) Harmonic approximation $p_{nl}(U_{ho})$, (b) Zeeman potential $p_{nl}(U_Z)$, and (c) cumulant $p_{nl}(\theta)$. We used $R = 40\,\mu m$ and $n_{max} = 3$, $l_{max} = 5$ in Eqs. (5), (2), and (8).

which is created by laser light far detuned from the atomic resonance. Here, $\Delta = \omega_L - \omega_0$ describes the laser detuning, and Ω_0 is the Rabi frequency. For red-detuned lasers $\omega_L < \omega_0$ with respect to the atomic transition ω_0, the dipole potential is attractive, and it is repulsive for blue-detuning $\omega_L > \omega_0$.[46]

For a single Laguerre–Gaussian beam,[47] the exponent $\theta(\boldsymbol{r})$ in Eq. (36) has the spatial dependence,

$$\theta(\boldsymbol{r}) = 2\frac{x^2 + y^2}{w(z)^2} + \ln\left(1 + \frac{z^2}{z_R^2}\right) \approx 2\frac{x^2 + y^2}{w_0^2} + \frac{z^2}{z_R^2}, \qquad (37)$$

where the Rayleigh range $z_R = \pi w_0^2/\lambda_L$ is typically much larger than the extension of the condensate wave packet. The laser wavelength is $\lambda_L = 2\pi/k_L$, and the beam waist is denoted by $w(z) = w_0(1 + z^2/z_R^2)^{1/2}$. The dipole potential Eq. (37) describes an optical waveguide[48] or can act as an optical matter-wave lens in the time domain.[49] For the latter, we depict the optical potential for ^{87}Rb in Fig. 3.

The harmonic approximation of Eq. (37) corresponds to the spheroidal trapping potential in Eq. (18) with stiffness

$$k_\perp = \frac{4U_0}{w_0^2}, \quad k_\parallel = \frac{2U_0}{z_R^2}, \qquad (38)$$

and the anisotropy $\alpha^2 = w_0^2/(2z_R)$ depending on the ratio of the minimal waist and the Rayleigh length.

As in Subsection III C, we evaluate the relative powers, see Fig. 4, for the harmonic approximation $p_{nl}(U_{ho})$ Eq. (18) (a), the dipole potential $p_{nl}(U_D)$ Eq. (36) (b), and the cumulant $p_{nl}(\theta)$ in Eq. (37) (c). Due to the Gaussian laser beam, the cumulant expansion of the dipole potential is much more efficient than the direct multipole expansion [compare Figs. 4(b) and 4(c)]. For large Rayleigh length $z_R \gg R$, the spatial dependence of the exponent $\theta(\boldsymbol{r})$ is almost Gaussian, which is shown in Figs. 4(a) and 4(b). Additional corrections to the harmonic cumulant in higher angular momentum components $l > 2$ are of the order 10^{-9} and smaller.

IV. MULTIPOLE EXPANSION OF BOSE–EINSTEIN CONDENSATES

In addition to the external trapping potentials, we are also interested in an efficient representation of a three-dimensional Bose–Einstein condensate. Within the classical field approximation for Bosons, the evolution of the complex matter-wave field is described,

$$i\hbar\partial_t \Psi(\boldsymbol{r}, t) = \left[-\frac{\hbar^2 \boldsymbol{\nabla}^2}{2M} + U(\boldsymbol{r}, t) + g n(\boldsymbol{r}, t)\right]\Psi(\boldsymbol{r}, t), \qquad (39)$$

$$N = \int d^3r\, n(\boldsymbol{r}, t), \qquad (40)$$

by the time-dependent Gross–Pitaevskii equation. Here, the contact-interaction strength is denoted by $g = 4\pi\hbar^2 a_s/M$, with the atomic mass M and the s-wave scattering length a_s. The atomic density $n(\boldsymbol{r}, t) = |\Psi(\boldsymbol{r}, t)|^2$ is normalized to the particle number N. Equivalenty to Eq. (39), one can represent the classical complex Gross–Pitaevskii field in terms of the two real hydrodynamical variables, the density of the condensates $n(\boldsymbol{r}, t)$ and its phase $\phi(\boldsymbol{r}, t)$,

$$\Psi(\boldsymbol{r}, t) = \sqrt{n(\boldsymbol{r}, t)}e^{i\phi(\boldsymbol{r}, t)}, \qquad (41)$$
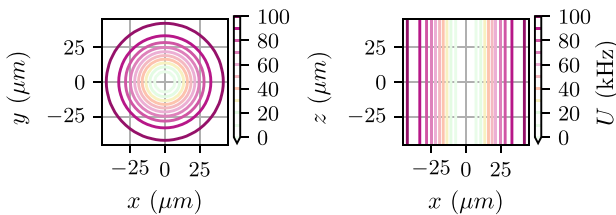
also known as a Madelung transform.[50]

Fɪɢ. 3. Optical dipole potential for a single Laguerre–Gaussian laser beam. Two-dimensional contour plots along all two spatial planes. Parameters of the trap as in Ref. 49, trap depth $|U_0|/k_B = 5\mu$K, Rayleigh range $z_R = 3.2$ mm, $w_0 = 33\,\mu$m, and the trapping frequencies $\boldsymbol{\nu} = (211.0\,, 211.0\,, 1.5)$ Hz for ^{87}Rb.
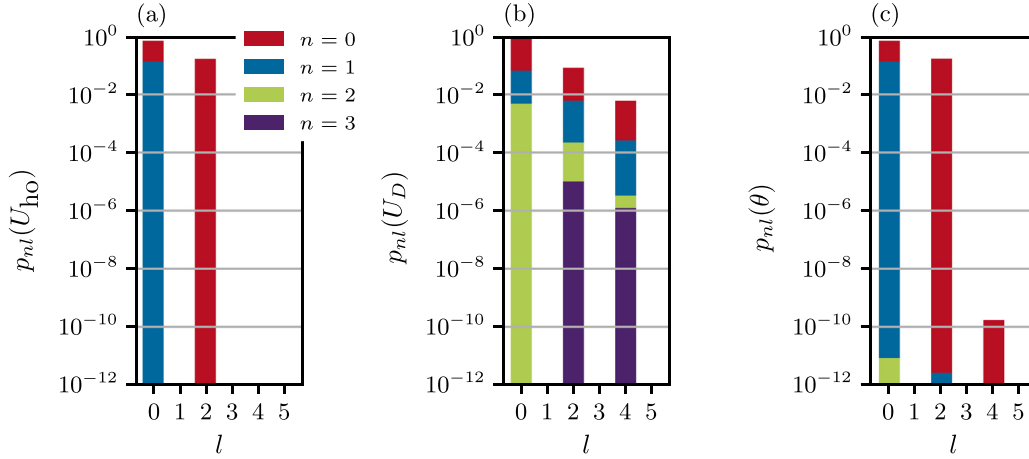
Fig. 4. Multipole expansion of the optical dipole potential for a single Laguerre–Gaussian beam shown in Fig. 3. Relative powers $p_{nl}(U)$ vs angular momentum l. Different principle numbers: red $n=0$, blue $n=1$, green $n=2$, and purple $n=3$. (a) Harmonic approximation $p_{nl}(U_{ho})$, (b) optical dipole potential $p_{nl}(U_D)$, and (c) cumulant $p_{nl}(\theta)$. We used $R=40\,\mu$m and $n_{max}=3$, $l_{max}=5$ in Eqs. (5), (2), and (8).

To represent the three-dimensional matter-wave field, we choose the same multipole expansion as in Eq. (2),

$$n(\mathbf{r}, t) = \sum_{n=0}^{\infty} \sum_{l=0}^{\infty} \sum_{m=-l}^{l} n_{nlm}(t) \langle \mathbf{r}|nlm \rangle, \qquad (42)$$

$$\phi(\mathbf{r}, t) = \sum_{n=0}^{\infty} \sum_{l=0}^{\infty} \sum_{m=-l}^{l} \phi_{nlm}(t) \langle \mathbf{r}|nlm \rangle, \qquad (43)$$

for the density as well as for the phase.

In the stationary case, the time-dependent field is governed by $\Psi(\mathbf{r}, t) = \Psi(\mathbf{r})e^{-i\mu t/\hbar}$, where $\mu(N)$ is the chemical potential of the condensate. Thus, the Gross–Pitaevskii equation for stationary field $\Psi(\mathbf{r})$ reads

$$\left[-\frac{\hbar^2 \mathbf{\nabla}^2}{2M} + U(\mathbf{r}) + gn(\mathbf{r}) \right] \Psi(\mathbf{r}) = \mu \Psi(\mathbf{r}). \qquad (44)$$

In the limit of large repulsive interactions, one can neglect the quantum pressure that arises from the localization energy of the classical field,

$$[U(\mathbf{r}) + gn_{TF}(\mathbf{r}) - \mu_{TF}]\Psi_{TF}(\mathbf{r}) = 0. \qquad (45)$$

Eq. (45) admits algebraic solutions of the form

$$n_{TF}(\mathbf{r}) = \begin{cases} \dfrac{\mu_{TF} - U(\mathbf{r})}{g}, & \mu_{TF} - U(\mathbf{r}) \geq 0, \\ 0 & \text{else}, \end{cases} \qquad (46)$$

known as the Thomas–Fermi approximation.[51]

In the following, we apply the multipole expansion in Eq. (42) for the condensate density in some of the trapping potentials discussed in Sec. III. Thereby, we discuss the strongly interacting Thomas–Fermi regime as well as the exact numerical solution of the stationary Gross–Pitaevskii equation.

We should note that in principle the Stringari polynomials in Eq. (42) can exhibit negative values, which are nonphysical when regarding positive-valued atomic densities. In order to avoid this anomaly, we consider coordinates in the interval $0 \leq r \leq R$ and densities $n(r) \geq 0$.

For the Thomas–Fermi density in Eq. (46), we expect an exact interpolation by the Stringari basis functions, if the potential is of polynomial form. In contrast, setting the interaction strength in Eq. (44) to $g=0$ and considering a harmonic oscillator potential, one obtains a Gaussian density distribution as the harmonic oscillator ground state,[35]

$$n(\mathbf{r}) = n_0\, e^{-\theta(\mathbf{r})}, \qquad \theta(\mathbf{r}) = \sum_{j=1}^{3} \frac{r_j^2}{2\sigma_j^2}. \qquad (47)$$

The widths of the Gaussian correspond to the harmonic oscillator lengths $\sigma_j = \sqrt{\hbar/(M\omega_j)}$, $j=1$, 2, and 3 for the three spatial directions. For the latter, the cumulant expansion

$$\theta(\mathbf{r}) = -\log \frac{n(\mathbf{r})}{n_0} = \sum_{n=0}^{\infty} \sum_{l=0}^{\infty} \sum_{m=-l}^{l} \theta_{nlm}\langle \mathbf{r}|nlm \rangle \qquad (48)$$

is always of a quadratic form. Thus, we recover the expansion coefficients for the optical dipole potential of a single Laguerre–Gaussian beam in Sec. III D.

A. Isotropic, three-dimensional density

We consider atomic density distributions in an isotropic harmonic oscillator potential (14). As the symmetry of the external potential determines the symmetry of the density, the condensate is interpolated by monopoles only. The efficiency of the interpolation depends on the actual radial shape $n(\mathbf{r}) = n(r)$, which will be determined by either the Thomas–Fermi density (46) or the stationary Gross–Pitaevskii equation (44). For the Gross–Pitaevskii density, we also evaluate the cumulant expansion to investigate the effect of different mean-field interactions.

1. Thomas–Fermi density

As the Thomas–Fermi density is directly proportional to the trapping potential, the interpolation is obtained by two Stringari

polynomials only, as discussed in Sec. III A. The Thomas–Fermi approximation in its dimensionless form is

$$n_{\text{TF}}(\boldsymbol{r}) = \frac{15N}{8\pi} n'(r'), \quad n'(r') = (1 - r'^2), \qquad (49)$$

with dimensionless radial coordinate $r' = r/r_{\text{TF}}$ and the Thomas–Fermi radius $r_{\text{TF}} = \sqrt{2\mu_{\text{TF}}(N)/(M\omega^2)}$. The chemical potential scales with the particle number as

$$\mu(N) = \frac{\hbar\omega}{2}\left(\frac{a_s N}{\ell}\right)^{2/5}, \quad \ell = \sqrt{\hbar/(M\omega)}. \qquad (50)$$

We find the monopole coefficients

$$n'_{000} = \frac{4}{5}\sqrt{\frac{\pi}{3}}, \quad n'_{100} = \frac{4}{5}\sqrt{\frac{\pi}{7}}. \qquad (51)$$

2. Gross–Pitaevskii density

We represent the three-dimensional matter-wave field on a discrete, Cartesian Fourier grid. Therefore, we solve the stationary Gross–Pitaevskii equation (44) using Fourier spectral methods. To study the behavior of the radial expansion coefficients in different interaction regimes, we choose different particle numbers for the condensate. The n_{nlm}'s in the multipole expansion of density in Eq. (42) are obtained using the method of least-squares [see Eq. (C2)] replacing the target potential with the numerical, discrete Gross–Pitaevskii target density $n_t(\boldsymbol{r}_j)$. In contrast to the Thomas-Fermi density, the radius $R = r_{\text{TF}}$ of the spherical integration volume in Eq. (5) is not known *a priori*. Therefore, we are minimizing the least-square error $\varepsilon(R)$ with respect to a variable aperture radius R,

$$\min \varepsilon(R) = ||\mathsf{S}(R)\boldsymbol{n} - \boldsymbol{n}_t||^2, \qquad (52)$$

for a fixed number of basis functions. The monopole coefficients $p_{n0}(n)$ for the isotropic Gross–Pitaevskii density are depicted in Fig. 5

on a semi-logarithmic scale for $n_{\max} = 14$ basis functions. For small particle numbers [Fig. 5(a)], the coefficients are declining exponentially for $n > 6$, whereas the magnitude of the tenth coefficient is $p_{10,0}(n) < 10^{-6}$. Entering the intermediate and strong interacting regime, the decline in magnitude becomes more irregular, as the Gaussian-like shape of the density is modified toward a polynomial shape. In Fig. 5(b), the most contributions to the polynomial expansion are within the first five coefficients, and in Fig. 5(c), within the first three. The latter reflects the transition to the pure quadratic Thomas–Fermi regime. However, we also recognize that the magnitude of the expansion coefficients does not converge to the same level as in the low interacting regime. In contrast to the Thomas–Fermi solution, the density also contains high-energetic modes close to the Thomas–Fermi radius, whose interpolation requires a lot of Stringari polynomials. As we are interested in good interpolation in the region of significant density, we introduce a cutoff at

$$p_{\text{c}} = \frac{|n_{nlm}|^2}{P(n)} = 10^{-6}, \quad P(n) = \sum_{nlm} |n_{nlm}|^2, \qquad (53)$$

which disregards some of the highly energetic modes. In Fig. 6, we plot the corresponding expansion in terms of the polynomials, which matches the Gross–Pitaevskii density quite well. We also use the Stringari polynomials with a reduced number of basis functions, neglecting coefficients smaller than the chosen cutoff.

In addition to the multipole coefficients for the density, we also look into the cumulant expansion in Eq. (8), for which we expect a faster convergence in the low-interacting limit. The $p_{n0}(\theta)$ in Fig. 7(a) confirm that the density distribution is more of a Gaussian shape, as the cumulant expansion almost terminates for monopole powers $n > 3$. For larger particle numbers, Figs. 7(b) and 7(c), the cumulant expansion works quite efficiently as the polynomial series converges faster as in Fig. 5. Cross sections of the cumulant and the interpolation with the Stringari polynomials are shown in Fig. 8.
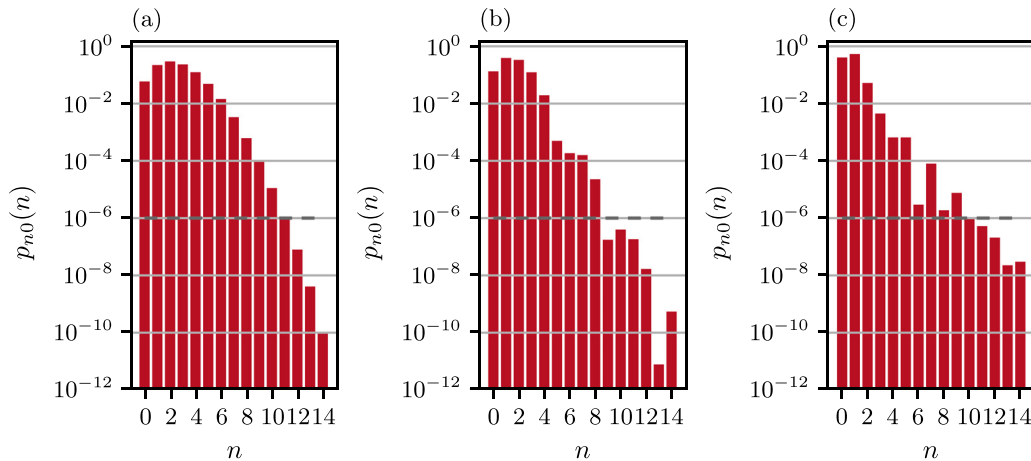

Fig. 5. Multipole expansion of the Gross–Pitaevskii density $n(\boldsymbol{r})$, Eq. (44), for the isotropic harmonic oscillator, Eq. (14). Monopole coefficients $p_{n0}(n)$ vs principle number n up to $n_{\max} = 14$. Parameters: trap frequency $\nu = 22.1\,\text{Hz}$, particle number, chemical potential, aperture radius R: (a) $N = 10$, $\mu/h = 35.6\,\text{Hz}$, and $R = 9.21\,\mu\text{m}$; (b) $N = 1000$, $\mu/h = 55.8\,\text{Hz}$, and $R = 8.95\,\mu\text{m}$; and (c) $N = 10^5$, $\mu/h = 289.2\,\text{Hz}$, and $R = 14.1\,\mu\text{m}$. For the reconstruction of the density in Fig. 6, we mark the cutoff $p_c = 10^{-6}$ (gray dashed line).
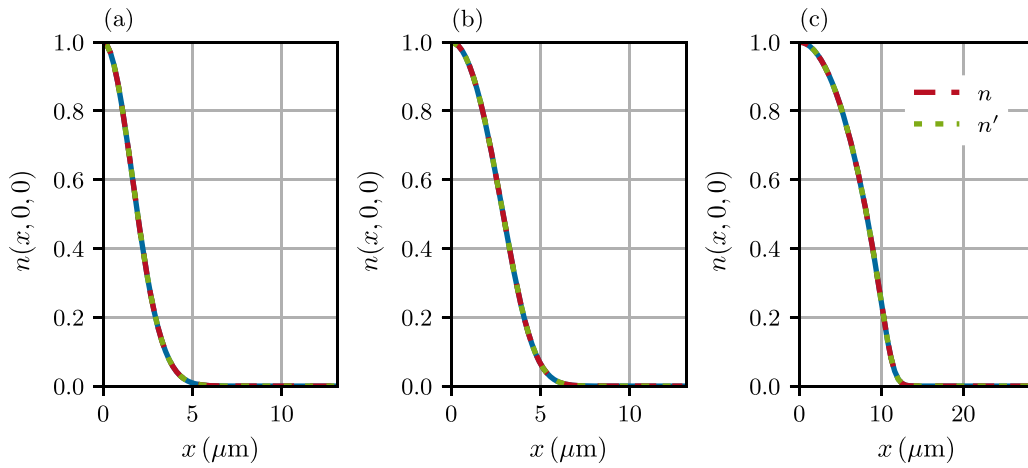
FIG. 6. Cross sections of the scaled Gross–Pitaevskii ground-state density distribution $n(x, 0, 0)$ vs the Cartesian coordinate x in a three-dimensional isotropic harmonic oscillator potential. Gross–Pitaevskii solution (blue solid line). Interpolation of the density with Stringari polynomials $n(r)$, Eq. (42), (red dashed line) and alternatively with the cutoff $\mathfrak{p}_c = 10^{-6}$ $n'(r)$ (green dotted line). Parameters: trap frequency $\nu = 22.1$ Hz, particle number, chemical potential, aperture radius R: (a) $N = 10$, $\mu/h = 35.6$ Hz, and $R = 9.21\,\mu$m; (b) $N = 1000$, $\mu/h = 55.8$ Hz, and $R = 8.95\,\mu$m; and (c) $N = 10^5$, $\mu/h = 289.2$ Hz, and $R = 14.1\,\mu$m.

B. Anisotropic three-dimensional density

As discussed in Ref. 52, the Thomas–Fermi field in a general harmonic oscillator potential can always be re-scaled to an isotropic s-wave by an affine coordinate transformation. Hence, this simplifies the search for the optimal aperture radius R and adapts the polynomial expansion on the finite interval to the anisotropic extension of the density distribution. The latter becomes necessary for an optimal and efficient interpolation of the Gross–Pitaevskii matter-wave field, which reaches beyond the Thomas-Fermi radius.

For this purpose, we evaluate the covariance matrix

$$\Sigma_r = \langle (r - r_0) \otimes (r - r_0) \rangle, \tag{54}$$

$$r_0 = \langle r \rangle = \int d^3 r\, r\, n(r), \tag{55}$$

for the three-dimensional Gross–Pitaevskii field. The positive, semi-definite matrix Σ_r admits a Cholesky decomposition of the form

$$\Sigma_r = CC^\top, \quad C = Q\sigma. \tag{56}$$

The matrices Q and σ are defined by the eigenvalue equation

$$\Sigma Q = Q\sigma^2. \tag{57}$$

The matrix C and the expectation value r_0 define the required affine coordinate transformation

$$\zeta = C^{-1}(r - r_0), \tag{58}$$

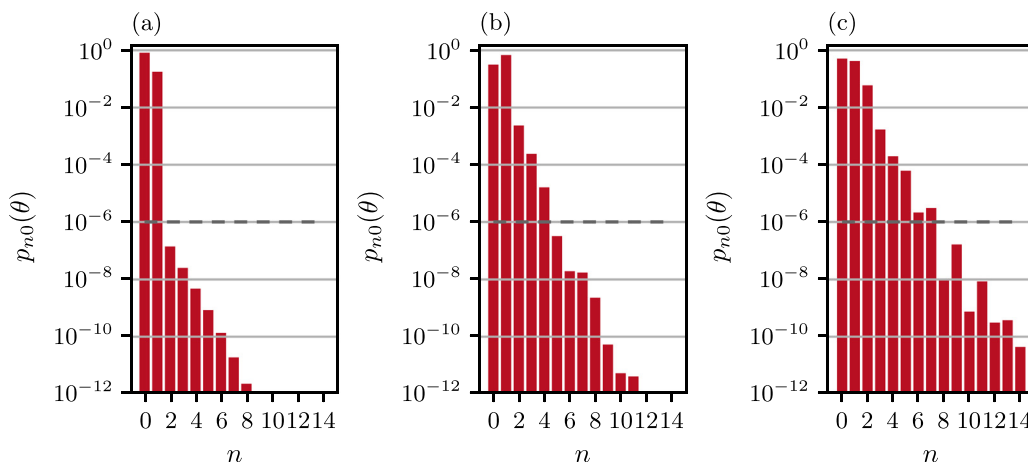that we use to evaluate a multipole expansion of the form

FIG. 7. Multipole expansion of the isotropic Gross–Pitaevskii cumulant $\theta(r)$, Eq. (48). Monopole coefficients $p_{n0}(\theta)$ vs principle number n with $n_{max} = 14$. For the reconstruction of the cumulant in Fig. 8, we mark the cutoff $p_c = 10^{-6}$ (gray dashed line). Parameters: trap frequency $\nu = 22.1$ Hz, particle number, chemical potential, aperture radius R: (a) $N = 10$, $\mu/h = 35.6$ Hz, and $R = 9.21\,\mu$m; (b) $N = 1000$, $\mu/h = 55.8$ Hz, and $R = 8.95\,\mu$m; and (c) $N = 10^5$, $\mu/h = 289.2$ Hz, and $R = 14.1\,\mu$m.
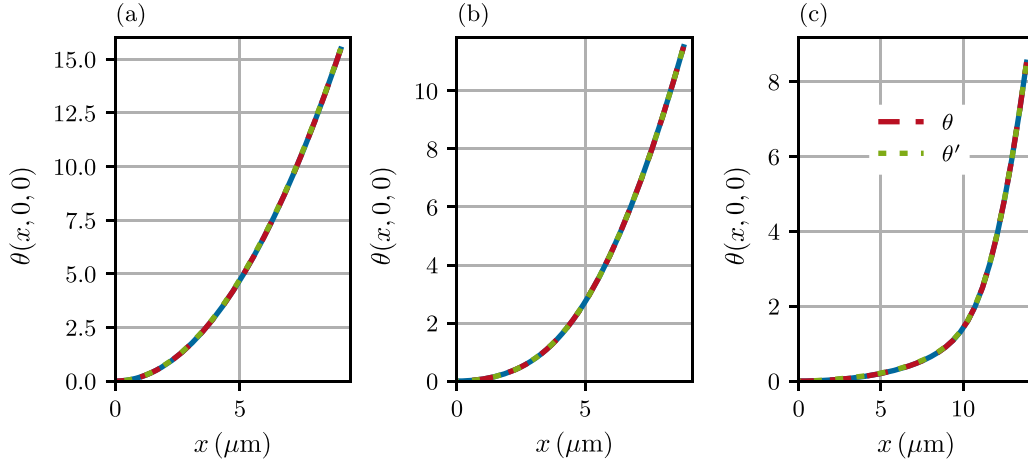
FIG. 8. Cross sections of the cumulant of the isotropic ground-state density distribution $\theta(x, 0, 0)$ vs the Cartesian coordinate x in a three-dimensional harmonic oscillator potential. Cumulant evaluated up to the aperture radius R. Gross–Pitaevskii solution (blue solid line), interpolation of the cumulant with Stringari polynomials θ (red dashed line) and alternatively with the cutoff $p_c = 10^{-6} \theta'$ (green dotted line). Parameters: trap frequency $\nu = 22.1$Hz, particle number, chemical potential, aperture radius R: (a) $N = 10$, $\mu/h = 35.6$ Hz, and $R = 9.21\,\mu m$; (b) $N = 1000$, $\mu/h = 55.8$ Hz, and $R = 8.95\,\mu m$; and (c) $N = 10^5$, $\mu/h = 289.2$ Hz, and $R = 14.1\,\mu m$.

$$n(\boldsymbol{r}) = \sum_{n=0}^{\infty}\sum_{l=0}^{\infty}\sum_{m=-l}^{l}\mathfrak{n}_{nlm}\langle\zeta|nlm\rangle,$$

$$\theta(\boldsymbol{r}) = \sum_{n=0}^{\infty}\sum_{l=0}^{\infty}\sum_{m=-l}^{l}\Theta_{nlm}\langle\zeta|nlm\rangle, \tag{59}$$

where the Stringari polynomials are evaluated with respect to the new coordinates ζ. For the new multipole coefficients $\mathfrak{n}_{nlm}$ and Θ_{nlm}, we define also the corresponding spectral powers,

$$\mathfrak{p}_{nl}(n) = \sum_{m=-l}^{l}\frac{|\mathfrak{n}_{nlm}|^2}{\mathfrak{P}(n)}, \quad \mathfrak{P}(n) = \sum_{nlm}|\mathfrak{n}_{nlm}|^2, \tag{60}$$

$$\mathfrak{p}_{nl}(\theta) = \sum_{m=-l}^{l}\frac{|\Theta_{nlm}|^2}{\mathfrak{P}(\theta)}, \quad \mathfrak{P}(\theta) = \sum_{nlm}|\Theta_{nlm}|^2. \tag{61}$$

1. Thomas–Fermi density. As a benchmark test, we investigate the Thomas–Fermi density in an anisotropic harmonic oscillator with cylindrical symmetry, which we discussed in Sec. III B 1. For the ratio of angular frequencies, we use $\alpha = 2$. From analyzing the potential, we know that the multipole expansion in Eq. (48) just exhibits monopoles as well as one quadrupole. Applying the coordinate transformation Eq. (58), we obtain the angular powers $\mathfrak{p}_{nl}(n_{\mathrm{TF}})$ shown in Fig. 9. As the multipole expansion is now performed in the scaled reference frame (59), where the ellipsoid is re-scaled to a sphere, we expect monopoles only, see Eq. (51). Indeed, we find good agreement with the isotropic Thomas–Fermi density as the quadrupoles are $\mathfrak{p}_{n2}(n_{\mathrm{TF}}) < 10^{-9}$ as displayed in Fig. 9. Using the monopoles $\mathfrak{n}_{n00}$ and the quadrupoles within the transformation matrix C, one can reconstruct the original oblate-shaped Thomas–Fermi density as depicted in Fig. 10.

2. Gross–Pitaevskii density. As in Sec. IV A 2, we study the interpolation of the Gross–Pitaevskii density for different particle numbers varying the effective mean-field interaction in Eq. (44). In addition, we

compare the multipole expansion of the density with the multipole expansion of the cumulant. In both cases, the expansion coefficients are evaluated in the scaled reference frame defined by Eq. (59). In contrast to the ellipsoidal Thomas–Fermi density, we observe non-negligible quadrupole contributions in the relative angular powers $\mathfrak{p}_{nl}(n)$ for the low as well as for the high interacting regime, which is presented in Fig. 11. For low particle numbers, Fig. 11(a), the angular powers $\mathfrak{p}_{n0}(n)$, $\mathfrak{p}_{n2}(n)$, and $\mathfrak{p}_{n4}(n)$ are decaying exponentially with respect to the principle number n as we already stated in the isotropic case. Increasing the angular momentum for a fixed value of n, the magnitudes of the $\mathfrak{p}_{nl}(n)$ decrease by roughly 1.5–2 orders of magnitude. The angular momentum dependence decreases for increasing interactions as shown in Figs. 11(b) and 11(c). In particular, the powers $\mathfrak{p}_{n4} < 10^{-6}$ are emphasizing the change of the Gross–Pitaevskii density toward the Thomas–Fermi shape. Moreover, the spectrum of the monopoles $\mathfrak{p}_{n0}(n)$ in the re-scaled reference frame exhibits the same structure as in the isotropic case (see Fig. 5), reflecting again the
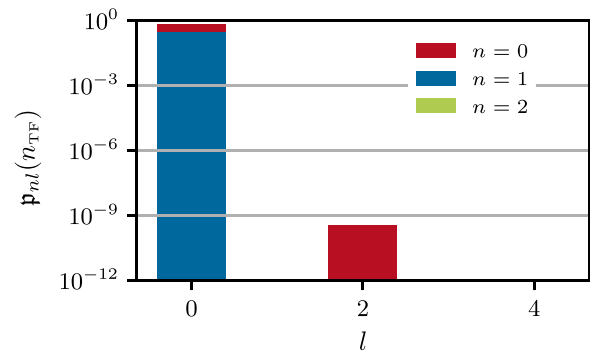

FIG. 9. Multipole expansion of the scaled Thomas–Fermi density $n_{\mathrm{TF}}(\boldsymbol{r})$ for the spheroidal harmonic oscillator, Eq. (18), with anisotropy $\alpha = 2$. Relative angular power $\mathfrak{p}_{nl}(n_{\mathrm{TF}})$ vs principle number n. Different principle numbers: red $n = 0$, blue $n = 1$, and green $n = 2$. $n_{\max} = 14$, $l_{\max} = 4$, and $R = 6.6\,\mu m$.
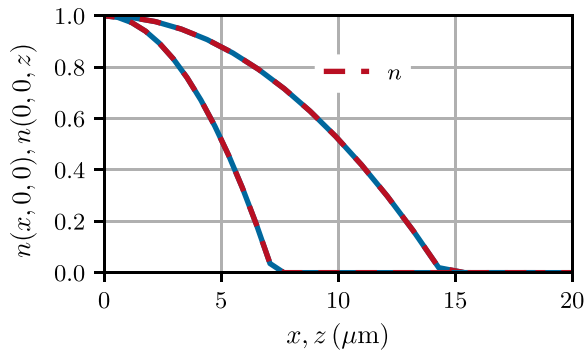
FIG. 10. Cross sections of the scaled Thomas–Fermi density $n_{TF}(x, 0, 0)$, $n_{TF}(0, 0, z)$ (blue solid line) vs Cartesian coordinates x, z in a spheroidal harmonic oscillator, Eq. (18). Interpolation of the density with Stringari polynomials $n(r)$, Eq. (42) (red dashed line). Parameters: $\alpha = 2$, Thomas–Fermi radii $x_{TF} = y_{TF} = 14.4 \mu$m, $z_{TF} = 7.2 \mu$m, particle number $N = 10^5$, chemical potential $\mu_{TF}/h = 304$ Hz.

high-energetic modes in the Gross–Pitaevskii density that require a large number of Stringari polynomials.

Nevertheless, we can interpolate the ground-state density distributions also in the anisotropic harmonic oscillator as depicted in Fig. 12. In particular, we can neglect modes with $l = 4$ for the condensate with large particle numbers to obtain a good approximation with the Stringari polynomials.

The results for the anisotropic cumulant expansion are presented in Figs. 13 and 14. The monopoles $\mathfrak{p}_{n0}(\theta)$ exhibit again the same features as for the isotropic density, while the cumulant expansion works more efficiently describing the low-interacting regime. The latter is well described by just three multipole coefficients Θ_{000}, Θ_{020} and, Θ_{200}, Fig. 13(a). In contrast to the direct multipole expansion of the density, the cumulant expansion contains significant angular powers $\mathfrak{p}_{n4}(\theta)$, which needs to be considered for the polynomial interpolation.

V. RELEASE AND FREE EXPANSION OF A BOSE–EINSTEIN CONDENSATE

Time of flight measurements is one of the standard techniques to image the density distribution of a Bose–Einstein condensate[53] after a ballistic expansion and to extract equilibrium as well as dynamical properties. Here, we investigate the release of the condensate initially trapped in the Zeeman potential of the magnetic chip trap that we characterized in Sec. III C.

Within the Thomas–Fermi approximation, Eq. (46), it is well-known[54–56] that the time evolution of the density $n_{TF}(\mathbf{r}, t)$ as well as the phase $\phi_{TF}(\mathbf{r}, t)$ is given in terms of the three adaptive scales $\lambda_j(t)$, $j = 1, 2, 3$,

$$n_{TF}(\mathbf{r}, t) = \frac{n_{TF}(\{r_j/\lambda_j(t)\}, 0)}{\lambda_1 \lambda_2 \lambda_3}, \tag{62}$$

$$\phi_{TF}(\mathbf{r}, t) = \frac{M}{2\hbar} \sum_{i=j}^{3} r_j^2 \frac{\dot{\lambda}_j(t)}{\lambda_j(t)}, \tag{63}$$

if the condensate is initially trapped in a harmonic trap. The adaptive scales evolve during the ballistic expansion according to the differential equations,

$$\ddot{\lambda}_j = \frac{\omega_j^2(0)}{\lambda_j \lambda_1 \lambda_2 \lambda_3}, \tag{64}$$

with initial conditions chosen as $\lambda_j(0) = 1$ and $\dot{\lambda}_j(0) = 0$. Therefore, the conjugate variables $n_{TF}(\mathbf{r}, t)$, $\phi_{TF}(\mathbf{r}, t)$ evolve quadratically in time, making the multipole expansions with the introduced Stringari polynomials in Eqs. (42) and (43) very efficient, as only monopoles as well as quadrupole contribute to Eqs. (42) and (43). Beyond, the Thomas–Fermi approximation, the initial Gross–Pitaevskii matter-wave field in the harmonic trap consists of non-quadratic polynomials,

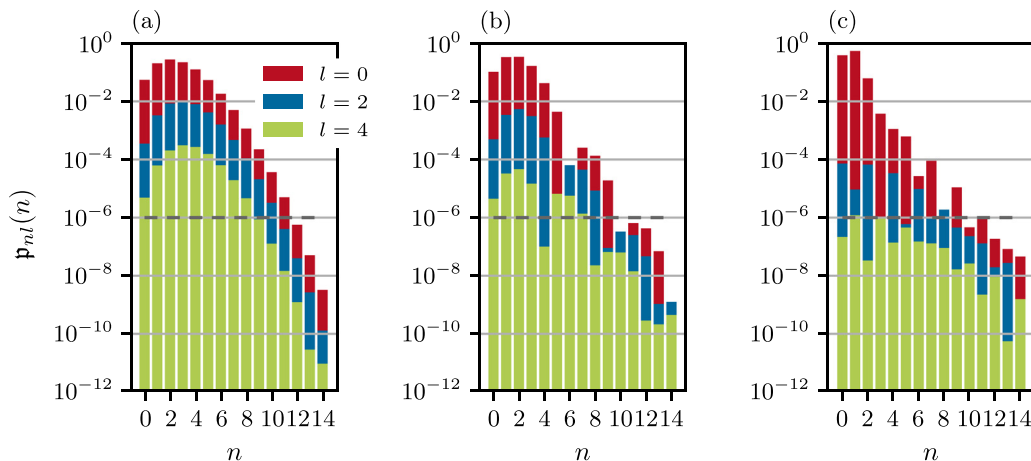$$n(\mathbf{r}) = n_{TF}(\mathbf{r}) + n_1(\mathbf{r}), \tag{65}$$

FIG. 11. Multipole expansion of the scaled Gross–Pitaevskii density $n(r)$, Eq. (44), for the spheroidal harmonic oscillator, Eq. (18), with anisotropy $\alpha = 2$. Relative angular powers $\mathfrak{p}_{nl}(n)$ vs principle number n. Different angular momenta: red $l = 0$, blue $l = 2$, and green $l = 4$, with $n_{max} = 14$, $l_{max} = 4$. For the reconstruction of the density in Fig. 12, we mark the cutoff $\mathfrak{p}_c = 10^{-6}$. Particle number, chemical potential, aperture radius: (a) $N = 10$, $\mu/h = 37.2$ Hz, and $R = 11.6 \mu$m; (b) $N = 1000$, $\mu/h = 60.6$ Hz, and $R = 12.1 \mu$m; and (c) $N = 10^5$, $\mu/h = 307$ Hz, $R = 17.6 \mu$m.
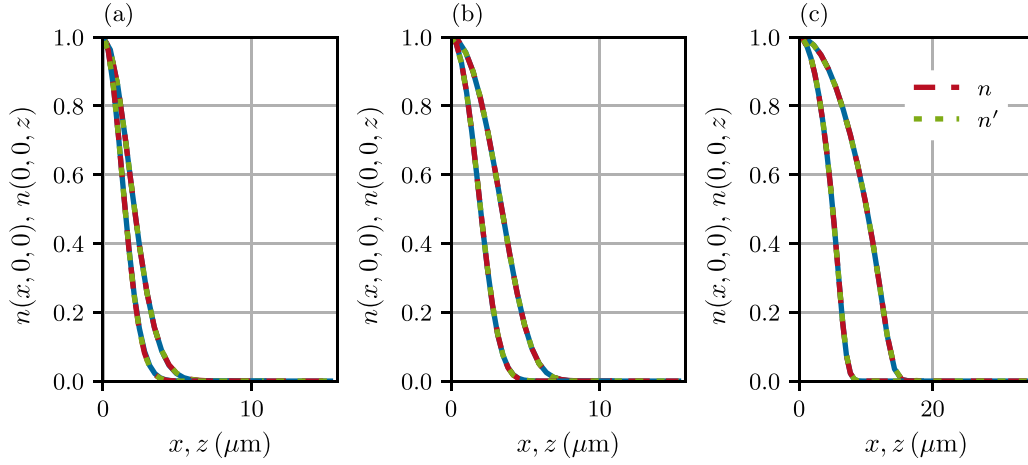
FIG. 12. Cross sections of the scaled ground-state density distributions $n(x, 0, 0)$, $n(0, 0, z)$ vs Cartesian coordinates x, z in a spheroidal harmonic oscillator, Eq. (18). Gross–Pitaevskii solution (blue solid line). Interpolation of the density with Stringari polynomials $n(\boldsymbol{r})$, Eq. (42) (red dashed line), alternatively with the cutoff $n'(\boldsymbol{r})$ at $\mathfrak{p}_c = 10^{-6}$ (green dotted line). Particle number, chemical potential, aperture radius: (a) $N = 10$, $\mu/h = 37.2$Hz, $R = 11.6 \mu m$; (b) $N = 1000$, $\mu/h = 60.6$ Hz, and $R = 12.1 \,\mu m$; (c) $N = 10^5$, $\mu/h = 307$ Hz, and $R = 17.6 \,\mu m$.

as analyzed numerically by our multipole expansion in Sec. IV and described analytically in Ref. 57. During the ballistic expansion of the condensate, the density deviation $n_1(\boldsymbol{r})$ leads to additional phase perturbations,

$$\phi(\boldsymbol{r}, t) = \phi_{\text{TF}}(\boldsymbol{r}, t) + \phi_1(\boldsymbol{r}, t), \qquad (66)$$

to the quadratic Thomas–Fermi phase ϕ_{TF} in Eq. (63). We obtain the total phase in Eq. (66) by solving the differential equation (64) for the adaptive scales $\lambda_j(t)$ and the Gross–Pitaevksii equation,

$$i\hbar\partial_t\psi(\boldsymbol{\xi}, t) = -\frac{\hbar^2}{2M} \sum_j \frac{1}{\lambda_j^2(t)} \partial_{\xi_j}^2 \psi(\boldsymbol{\xi}, t)$$
$$+ \frac{1}{\lambda_1\lambda_2\lambda_3}\left(\frac{M}{2}\sum_j \omega_j^2(0)\xi_j^2 + gn(\boldsymbol{\xi}, t) - \mu\right)\psi(\boldsymbol{\xi}, t),$$

$$(67)$$

in the co-expanding frame of reference with the coordinates $\xi_j = r_j/\lambda_j(t)$. The transformed field $\psi(\boldsymbol{\xi}, t)$ is related to the original one in Eq. (39) by
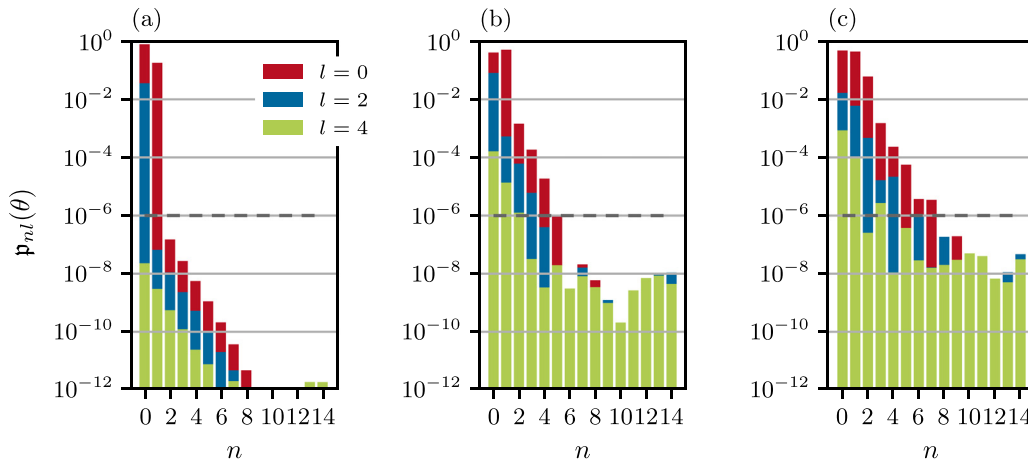

FIG. 13. Multipole expansion of the Gross–Pitaevskii cumulant $\theta(\boldsymbol{r})$, Eq. (48), for the spheroidal harmonic oscillator, Eq. (18), with anisotropy $\alpha = 2$. Relative angular powers $\mathfrak{p}_{nl}(\theta)$ vs principle number n. Different angular momenta: red $l = 0$, blue $l = 2$, and green $l = 4$, with $n_{max} = 14$, $l_{max} = 4$. For the reconstruction of the cumulant in Fig. 14, we mark the cutoff $\mathfrak{p}_c = 10^{-6}$ (gray dotted line). Particle number, chemical potential, aperture radius: (a) $N = 10$, $\mu/h = 37.2$ Hz, and $R = 11.6 \mu m$; (b) $N = 1000$, $\mu/h = 60.6$ Hz, and $R = 12.1 \,\mu m$; and (c) $N = 10^5$, $\mu/h = 307$ Hz, and $R = 17.6 \,\mu m$.
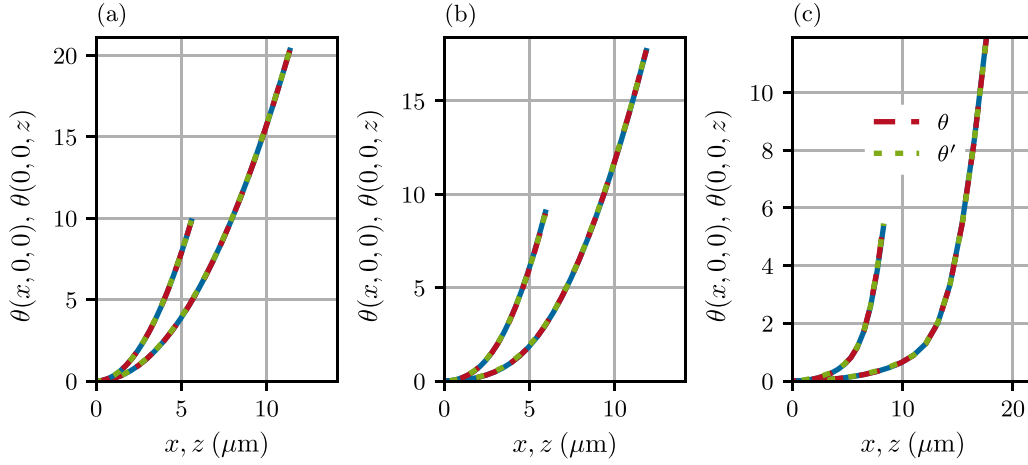
FIG. 14. Cross section of the cumulants $\theta(x, 0, 0)$, $\theta(0, 0, z)$ of the ground-state density distribution vs Cartesian coordinates x, z in a spheroidal harmonic oscillator Eq. (18). Cumulant evaluated up to the aperture radius R. Gross–Pitaevskii solution (blue solid line). Interpolation of the cumulant with Stringari polynomials $\theta(\mathbf{r})$ Eq. (8) (red dotted line), alternatively with the cutoff $\theta'(\mathbf{r})$ at $\mathfrak{p}_c = 10^{-6}$ (green dashed line). Particle number, chemical potential, aperture radius: (a) $N = 10$, $\mu/h = 37.2$ Hz, and $R = 11.6\,\mu$m; (b) $N = 1000$, $\mu/h = 60.6$ Hz, and $R = 12.1\,\mu$m; (c) $N = 10^5$, $\mu/h = 307$ Hz, and $R = 17.6\,\mu$m.

$$\Psi(\mathbf{r}, t) = \frac{1}{\sqrt{\lambda_1 \lambda_2 \lambda_3}} \psi(\boldsymbol{\xi}, t) e^{i[\phi_{\mathrm{TF}}(\boldsymbol{\xi}, t) - \beta(t)]}, \quad (68)$$

$$\beta(t) = \int^t \frac{dt'}{\hbar} \frac{\mu}{\lambda_1 \lambda_2 \lambda_3}. \quad (69)$$

At $t = 0$, the field $\psi(\boldsymbol{\xi}, 0)$ satisfies the stationary Gross–Pitaevskii equation (44) with $N = 10^5$ ^{87}Rb atoms. As an external potential $U(\mathbf{r})$, we choose the Zeeman potential U_Z as well as the harmonic approximation. For the chosen parameter, we find the Thomas–Fermi size $\mathbf{r}_{\mathrm{TF}} = (25.5, 8.3, 9.4)\,\mu$m and maximal density deviations of max $\delta n = 0.1\%$ within the two different trapping configurations.

To analyze the impact on the phase during the ballistic expansion after a flight of flight $t_1 = 80$ms, we apply the multipole expansion of the total phase in Eq. (66) with respect to the re-scaled coordinates $\boldsymbol{\xi}$ for these two different initial states. The relative angular powers $p_{nl}(\phi)$,

$$p_{nl}(\phi) = \sum_{m=-l}^{l} \frac{|\phi_{nlm}|^2}{P(\phi)}, \quad P(\phi) = \sum_{nlm} |\phi_{nlm}|^2, \quad (70)$$

are shown in Fig. 15. In the two subfigures, we compare the phase of the condensate that was initially trapped in the Zeeman potential (a) to the condensate initially in the harmonic approximation (b). From the latter, we state that the next leading orders to the scaling approximation (63) are of the form r^4 with spectral powers $p_{20}(\phi)$, $p_{12}(\phi)$, and $p_{04}(\phi)$. In addition, we find that their values are approximately three orders of magnitude higher than the anharmonic corrections, which populate the dipole $p_{n1}(\phi)$ and the octupole moments $p_{n3}(\phi)$ in the phase of the condensate.

VI. COMPUTATIONAL VERSUS DATA EFFICIENCY

Choosing good basis states is important for efficient computations with real trapping potentials or complex wave functions. Unfortunately, no single best basis can be identified that suits all other purposes equally well.

This was studied for the Zeeman potential of an atomic chip in Sec. III C, for the optical dipole potential in Sec. III D and for the interacting BEC with varying particle number in Secs. IV A and IV B. By comparing the direct multipole expansions to the cumulant series
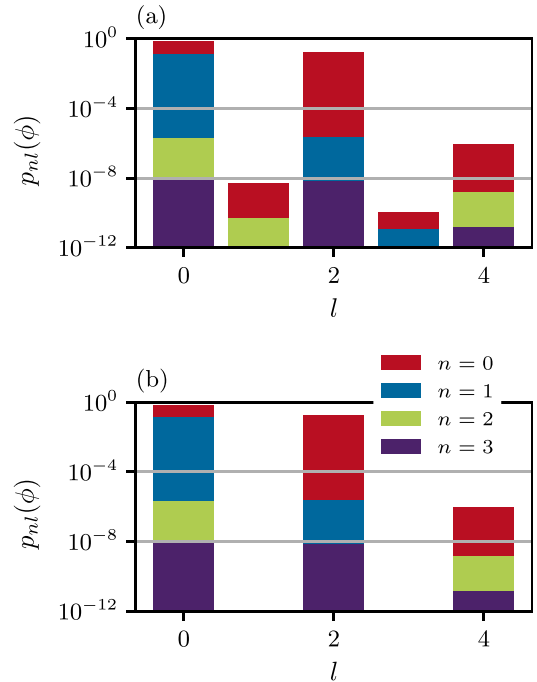
FIG. 15. Multipole expansion of the phase $\phi(\mathbf{r}, t_1)$, Eq. (66), of an expanding Bose–Einstein condensate after $t_1 = 80$ ms time-of-flight. Relative angular powers $p_{nl}(\phi)$, Eq. (70), vs angular momentum l. (a) condensate initially trapped in the Zeeman potential (see Sec. III C) of an atom chip, (b) condensate initially trapped in the anisotropic harmonic approximation of the Zeeman potential, Eq. (22). Parameters of the trap as in Table II. Different principle numbers: red $n = 0$, blue $n = 1$, green $n = 2$, purple $n = 3$, with $n_{\max} = 3$, $l_{\max} = 4$.

multipole expansion,[32] which favors Gaussian states, we demonstrated in Fig. 4 that the dipole potential of the Gauss–Laguerre laser beam is better represented by the cumulant series than the direct multipole expansion. The analogous behavior was discussed in Fig. 7, which shows that Gaussian states represent weakly interacting condensates very well, while a few Stringari polynomials are the better choice for the strongly interacting case. Thus, a prudent choice of a set of basis states $\{|u_i\rangle\}$ results in a data-efficient representation with only a few amplitudes.

Another objective for a choice of basis states is the flexibility to represent experimental situations without symmetries or depending on the requirements of numerical algorithms. Typical split-step codes for the numerical solution of time-dependent three-dimensional Schrödinger-type equations rely intimately on the position representation $\{|v_j\rangle\}$ for the action of local potentials and the Fourier representation $\{|w_k\rangle\}$ for the kinetic evolution. Thus, a given trial wave-function $|\psi\rangle$ can be decomposed in multiple ways,

$$|\psi\rangle = \sum_i |u_i\rangle\langle u_i|\psi\rangle = \sum_j |v_j\rangle\langle v_j|\psi\rangle = \sum_k |w_k\rangle\langle w_k|\psi\rangle. \quad (71)$$

When the local operator (LO) has performed numerical simulations on the available hardware (CPU, GPU, memory), he has to process the data to extract the information from it. This information has to be shared with the peers over classical communication (CC) channels. In the past, CC was a printed article with colored two-dimensional view-graphs. In the present, CC can be the information on the shape of the trapping potential on the up-link channel for space-borne experiments like the MAIUS mission[58] or the CAL experiment[59] on the International Space Station. This protocol is known as LOCC in quantum communication.

The efficiency of the data representation of a state depends on the spread of the state-occupation $p_i = |\langle u_i|\psi\rangle|^2$ in N-dimensional Hilbert-space. For a normalized state $\sum_i p_i = 1$, the Shannon-entropy,

$$S = \sum_i p_i \log_2(1/p_i), \quad (72)$$

is a measure of the efficiency of a representation. On one hand, if one picks the ideal communication basis, which matches the trial wave function $|\psi\rangle = |u_1\rangle$ perfectly, there is no uncertainty $S = 0$. On the other hand, in the computational position basis $|v_j\rangle$, state-occupations will spread out in Hilbert space, in the extreme limit, even completely homogeneously $p_j = |\langle v_j|\psi\rangle|^2 = 1/N$. This maximizes the uncertainty $S = \log_2(N)$.

For our simulation of the ballistically expanding BEC in Sec. V, we use three-dimensional Cartesian grids with $N = (2^8)^3 = 16.8 \times 10^6$ points. Then, a time-dependent wave function $\psi(x, y, z, t)$ is a four-dimensional field of complex double precision numbers (32 byte). At one instant, this is 0.5GB. This has to be compared to $\sim 2(n < 4)(l < 5)(|m| \leq l) = 200$ complex multipole coefficients (n_{nlm}, ϕ_{nlm}) that capture the same information, shown in Fig. 15. This is data efficient.

VII. CONCLUSION AND OUTLOOK

In conclusion, we have introduced a multipole expansion with suitable radial polynomials to characterize different trapping geometries and the matter-wave field of a three-dimensional Bose–Einstein condensate. In addition to the optical dipole potential for a single Laguerre–Gaussian beam, we have examined the multipole moments for the Zeeman potential of a realistic atom chip model. For both, we quantified deviations from their harmonic approximation and introduced an expansion of the cumulant, which is superior for Gaussian-shaped functions. In the Thomas–Fermi approximation, the shape of the condensate is directly proportional to the external potential. Hence, it is natural to characterize the three-dimensional shapes of density and phase in terms of the same polynomial basis functions. Moreover, we have examined the efficiency of our multipole expansion for the different mean-field interactions in the Gross–Pitaevskii equation. In addition, we studied the phase of an expanding condensate in the same manner. We identified possible aberrations for long-time atom interferometry in the different multipole moments that are caused either by the external potentials or the intrinsic properties of interacting Bose–Einstein condensates.

Our work provides a general and universal framework for an aberration analysis in matter-wave optics with interacting Bose–Einstein condensates. The multipole analysis allows the design for aberration balanced matter-wave lenses in single or multiple lens set-ups,[40,49] e.g., with programable optical dipole potentials using digital micromirror devices.[60] Finally, the multipole expansion of the magnetic field could be used to exploit different trapping geometries and for designing new atom chips.[61]

AUTHOR DECLARATIONS
Conflict of Interest

The authors have no conflicts to disclose.

Author Contributions

Jan Teske: Writing – original draft (lead); Writing – review & editing (equal). **Reinhold Walser:** Writing – original draft (supporting); Writing – review & editing (equal).

DATA AVAILABILITY

The data that support the findings of this study are available from the corresponding author upon reasonable request.

APPENDIX A: JACOBI POLYNOMIALS

The Jacobi polynomials are defined by a Gaussian hypergeometric function $_2F_1(a, \alpha, \beta)$[28] for integer values $a = -n$,

04 March 2024 12:38:33

$$J_n^{(\alpha,\beta)}(x) = \frac{(\alpha+1)_n}{n!} \times {}_2F_1\left(-n, n+\alpha+\beta+1; \alpha+1; \frac{1-x}{2}\right), \quad (A1)$$

where $(\cdot)_n$ denotes the Pochhammer symbol. They are orthogonal on the interval $x \in [-1, 1]$,

$$\int_1^1 dx\, w_{\alpha,\beta}(x) J_n^{(\alpha,\beta)}(x) J_m^{(\alpha,\beta)}(x) = \mathscr{A}_n \delta_{n,m}, \quad (A2)$$

$$\mathscr{A}_n = \frac{2^{\alpha+\beta+1}}{2n+\alpha+\beta+1} \frac{\Gamma(n+\alpha+1)\Gamma(n+\beta+1)}{\Gamma(n+\alpha+\beta+1)n!}, \quad (A3)$$

with respect to the weight function

$$w_{\alpha,\beta}(x) = (1-x)^\alpha (1+x)^\beta. \quad (A4)$$

The Stringari polynomials in Eq. (5) are shifted Jacobi polynomials with $\alpha = l + 1/2$ and $\beta = 0$ substituting the coordinate as $x = 1 - 2(r/R)^2$, $r \in [0, R]$. The normalization constant $\mathscr{N}_{nl}$ in Eq. (5) is obtained by using Eq. (A3).

APPENDIX B: MAGNETIC TRAPPING ON AN ATOM CHIP

The atom chip model is a representation of the experiment[43] and is shown in Fig. 16. The chip consists of three isolated conducting layers providing several possible trapping configurations. The first layer holds the largest mesoscopic structures. The U-shaped wires form a quadrupole field that is used for the three-dimensional magneto-optical trap (MOT). The second layer, the base chip (BC), and the third layer, the science chip (SC), consist of four- and five-wire two-dimensional strips, respectively, which intersect with one central orthogonal wire. We regard the active conductors on the base as well as on the science chip in Z-trap configuration, which are marked in red and blue colors in Fig. 16. Both create an Ioffe–Pritchard-type trapping potential that is used for releasing and collimating the condensate. The field is superposed by a magnetic bias field $\boldsymbol{B}_0$ created by three pairs of Helmholtz coils.
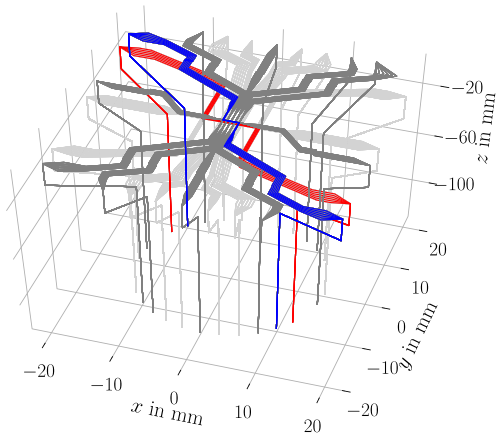

FIG. 16. QUANTUS II atom chip model as described in Refs. 43, and 62. Light-gray wires belong to the base chip structure. Gray wires belong to the science chip structure. Active conductors in Z-trap configuration in blue (science chip) and red (base chip) colors. External Helmholtz coils creating a homogeneous field are not depicted.
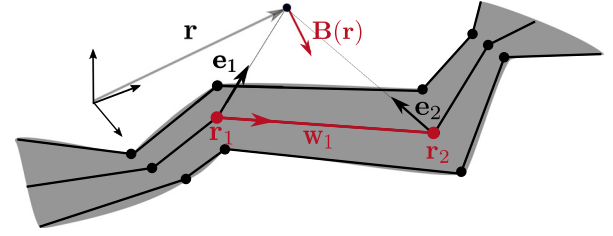

FIG. 17. Subsection with $N = 5$ segments from a finite two-dimensional conducting strip of the QUANTUS II atom chip in Fig. 16. Each segment is modeled by M finite wires, here $M = 3$. The magnetic induction $\boldsymbol{B}(\boldsymbol{r})$ at an observation point $\boldsymbol{r}$ created by a current I_i in the finite wire element pointing into direction $\boldsymbol{w}_1$.

TABLE I. Typical set of currents applied to the atom chip to generate a magnetic trap.

Wire	Current
Science chip	2.0A
Base chip	6.0A
x-coils	0.1A
y-coils	−0.37431A
z-coils	0.0A

The magnetic induction field $\boldsymbol{B}_c$ of the atom chip is calculated by splitting N two-dimensional wire strip segments into M finite wire elements (cf. Fig. 17) that describe the shape of all wire strips in all layers. We use finite wires with lengths $l_i = |\boldsymbol{r}_2^{(i)} - \boldsymbol{r}_1^{(i)}|$ that point into the directions $\boldsymbol{w}^{(i)} = (\boldsymbol{r}_2^{(i)} - \boldsymbol{r}_1^{(i)})/l_i$ and carry a steady current $I_i = I/M$, where M is the number of wires representing a segment i (see Fig. 17). The magnetic induction for a single finite wire element follows from the Biot–Savart law[63] using the parametrization of one wire $\boldsymbol{r}'(s) = \boldsymbol{r}_1 + \boldsymbol{w}ls$, $s \in [0, 1]$,

$$\boldsymbol{B}_c(\boldsymbol{r}) = \frac{\mu_0}{4\pi} \frac{I}{\rho} \frac{\boldsymbol{e}_1 \times \boldsymbol{w}}{1 - (\boldsymbol{e}_1 \cdot \boldsymbol{w})^2} (\boldsymbol{e}_2 - \boldsymbol{e}_1) \cdot \boldsymbol{w}, \quad (B1)$$

where the unit vectors $\boldsymbol{e}_2$, $(\boldsymbol{e}_1)$ are pointing from the conductor's end (start) to the observation point $\boldsymbol{r}$, and $\rho = |\boldsymbol{r} - \boldsymbol{r}_1|$ denotes the distance to the head of the wire element at $\boldsymbol{r}_1$. Hence, the total magnetic induction field of M wires in N segments is just the sum of all individual fields,

$$\boldsymbol{B}(\boldsymbol{r}) = \boldsymbol{B}_0 + \sum_{i=1}^{NM} \boldsymbol{B}_c^{(i)}(\boldsymbol{r}),$$

$$\boldsymbol{B}_c^{(i)}(\boldsymbol{r}) = \frac{\mu_0}{4\pi} \frac{I_i}{\rho_i} \frac{\boldsymbol{e}_1^{(i)} \times \boldsymbol{w}^{(i)}}{1 - (\boldsymbol{e}_1^{(i)} \cdot \boldsymbol{w}^{(i)})^2} \left(\boldsymbol{e}_2^{(i)} - \boldsymbol{e}_1^{(i)}\right) \cdot \boldsymbol{w}^{(i)}. \quad (B2)$$

APPENDIX C: NUMERICAL EVALUATION

While the multipole coefficients may be evaluated analytically using the scalar product in Eq. (7), we are using a least-square evaluation[64] when the potential is represented on a numerical grid. As the discretized Stringari polynomials are non-orthogonal basis functions, we introduce the finite complex scalar product

04 March 2024 12:38:33

TABLE II. Physical parameters of the QUANTUS II release trap. Spring constants and trap frequencies are corresponding to the magnetic substate $|F = 2, m_F = 2\rangle$. Tilt angles are evaluated in the chip coordinate system.

Parameter	Symbol	Value
Spring constant	$\boldsymbol{k}$	$(709, 6685, 5210)$ kHz mm^{-2}
Frequencies ^{87}Rb	$\boldsymbol{\nu}_{\mathrm{Rb}}$	$(9.08, 27.88, 24.61)$ Hz
Frequencies ^{41}K	$\boldsymbol{\nu}_{\mathrm{K}}$	$(13.23, 40.41, 35.86)$ Hz
Trap minimum	$\boldsymbol{r}_0$	$(0, 0, 1462)$ μm
Tait–Bryan angles (XYZ)	α, β, γ	$(0., 0, 9.7)^\circ$

$$(a|b) = \sum_{\boldsymbol{r}_j \in V} \mathscr{V} a^*(\boldsymbol{r}_j) b(\boldsymbol{r}_j) = \boldsymbol{a}^\dagger \boldsymbol{b}, \tag{C1}$$

with the discrete position coordinates $\{\boldsymbol{r}_j\}$, the measure of the Cartesian volume element $\mathscr{V} = \Delta x \Delta y \Delta z$, and its norm $||\boldsymbol{a}|| = \sqrt{(a|a)}$. Hence, the distance of the squared residuals is given by

$$\varepsilon = ||\mathsf{S}\boldsymbol{u} - \boldsymbol{U}||^2. \tag{C2}$$

Here, we have introduced the complex coefficient vector $\boldsymbol{u} = \{U_{nlm}\}$, the values of the discrete target potential $\boldsymbol{U} = \{U(\boldsymbol{r}_j)\}$, and the complex matrix $\mathsf{S} = \{S_{nlm}(\boldsymbol{r}_j)\}$ that contains the discrete set of the finite Stringari basis functions. One finds the least square minimum

$$\partial \varepsilon / \partial \boldsymbol{u}^* = 0, \tag{C3}$$

which leads to the best potential parameter estimate

$$\bar{\boldsymbol{u}} = (\mathsf{S}^\dagger \mathsf{S})^{-1} \mathsf{S}^\dagger \boldsymbol{U}. \tag{C4}$$

REFERENCES

[1] F. Zernike, Physica **1**, 689–704 (1934).
[2] F. Zernike, "Das Phasenkontrastverfahren bei der mikroskopischen Beobachtung," Z. Techn. Phys. **16**, 454 (1935).
[3] *Handbook of Optical Systems: Volume 1: Fundamentals of Technical Optics*, 1st ed., edited by H. Gross (Wiley, 2005).
[4] *Handbook of Optical Systems: Volume 3: Aberration Theory and Correction of Optical Systems*, edited by H. Gross, H. Zügge, M. Peschka, and F. Blechinger (Wiley-VCH Verlag GmbH & Co. KGaA, Weinheim, Germany, 2006).
[5] M. Haider, S. Uhlemann, E. Schwan, H. Rose, B. Kabius, and K. Urban, Nature **392**, 768 (1998).
[6] P. E. Batson, N. Dellby, and O. L. Krivanek, Nature **418**, 617 (2002).
[7] D. A. Muller, L. F. Kourkoutis, M. Murfitt, J. H. Song, H. Y. Hwang, J. Silcox, N. Dellby, and O. L. Krivanek, Science **319**, 1073 (2008).
[8] H. H. Rose, *Geometrical Charged-Particle Optics*, Springer Series in Optical Sciences Vol. 142 (Springer Berlin Heidelberg, Berlin, Heidelberg, 2009).
[9] A. D. Cronin, J. Schmiedmayer, and D. E. Pritchard, Rev. Mod. Phys. **81**, 1051 (2009).
[10] W. Ertmer, C. Schubert, T. Wendrich, M. Gilowski, M. Zaiser, T. V. Zoest, E. Rasel, C. J. Bordé, A. Clairon et al., Exp. Astron. **23**, 611–649 (2009).
[11] D. Schlippert, J. Hartwig, H. Albers, L. L. Richardson, C. Schubert, A. Roura, W. P. Schleich, W. Ertmer, and E. M. Rasel, Phys. Rev. Lett. **112**, 203002 (2014).
[12] O. Gabel, "Bose-Einstein condensates in curved space-time: From concepts of general relativity to tidal corrections for quantum gases in local frames," Ph.D. thesis (Technische Universität Darmstadt, 2019).
[13] T. Kovachy, P. Asenbaum, C. Overstreet, C. A. Donnelly, S. M. Dickerson, A. Sugarbaker, J. M. Hogan, and M. A. Kasevich, Nature **528**, 530 (2015).
[14] Y. A. El-Neaj, C. Alpigiani, S. Amairi-Pyka, H. Araújo, A. Balaž, A. Bassi, L. Bathe-Peters, B. Battelier, A. Belić et al., EPJ Quantum Technol. **7**, 6 (2020).
[15] S. Dimopoulos, P. W. Graham, J. M. Hogan, M. A. Kasevich, and S. Rajendran, Phys. Lett. B **678**, 37 (2009).
[16] G. M. Tino, A. Bassi, G. Bianco, K. Bongs, P. Bouyer, L. Cacciapuoti, S. Capozziello, X. Chen, M. L. Chiofalo et al., Eur. Phys. J. D **73**, 228 (2019).
[17] K. S. Thorne, Rev. Mod. Phys. **52**, 299 (1980).
[18] K. S. Thorne, Rev. Mod. Phys. **90**, 040503 (2018).
[19] K. Bongs, M. Holynski, J. Vovrosh, P. Bouyer, G. Condon, E. Rasel, C. Schubert, W. P. Schleich, and A. Roura, Nat. Rev. Phys. **1**, 731 (2019).
[20] G. Nandi, R. Walser, E. Kajari, and W. P. Schleich, Phys. Rev. A **76**, 063617 (2007).
[21] A. Neumann, M. Gebbe, and R. Walser, Phys. Rev. A **103**, 043306 (2021).
[22] A. Neumann, "Aberrations of atomic diffraction—From ultracold atoms to hot ions," Ph.D. thesis (Technische Universität Darmstadt, 2021).
[23] M. Cornelius, "Atom interferometry with picokelvin ensembles in microgravity," Ph.D. thesis (Universität Bremen, 2022).
[24] H. J. Metcalf and P. van der Straten, "*Laser cooling and trapping*," in *Graduate Texts in Contemporary Physics*, edited by R. S. Berry, J. L. Birman, J. W. Lynn, M. P. Silverman, H. E. Stanley, and M. Voloshin (Springer New York, New York, NY, 1999).
[25] Ł. Dobrek, M. Gajda, M. Lewenstein, K. Sengstock, G. Birkl, and W. Ertmer, Phys. Rev. A **60**, R3381 (1999).
[26] H. Ammann and N. Christensen, Phys. Rev. Lett. **78**, 2088 (1997).
[27] S. Abend, B. Allard, A. S. Arnold, T. Ban, L. Barry, B. Battelier, A. Bawamia, Q. Beaufils, S. Bernon et al., AVS Quantum Sci. **5**, 019201 (2023).
[28] F. W. Olver, D. W. Lozier, R. F. Boisvert, and C. W. Clark, *NIST Handbook of Mathematical Functions*, 1st ed. (Cambridge University Press, USA, 2010).
[29] S. Stringari, Phys. Rev. Lett. **77**, 2360 (1996).
[30] P. Öhberg, E. L. Surkov, I. Tittonen, S. Stenholm, M. Wilkens, and G. V. Shlyapnikov, Phys. Rev. A **56**, R3346 (1997).
[31] M. Born, E. Wolf, A. B. Bhatia, P. C. Clemmow, D. Gabor, A. R. Stokes, A. M. Taylor, P. A. Wayman, and W. L. Wilcock, *Principles of Optics: Electromagnetic Theory of Propagation, Interference and Diffraction of Light*, 7th ed. (Cambridge University Press, 1999).
[32] C. W. Gardiner, *Handbook of Stochastic Methods for Physics, Chemistry, and the Natural Sciences* (Springer, 1985).
[33] D. A. Varshalovich, A. N. Moskalev, and V. K. Khersonskii, *Quantum Theory of Angular Momentum* (World Scientific, 1988).
[34] L. E. Ballentine, *Quantum Mechanics: A Modern Development*, 2nd ed. (World Scientific, 2014).
[35] A. Galindo and P. Pascual, *Quantum Mechanics I* (Springer Berlin Heidelberg, Berlin, Heidelberg, 1990).
[36] A. R. Edmonds, *Angular Momentum in Quantum Mechanics* (Princeton University Press, 1957).
[37] T. Bergeman, G. Erez, and H. J. Metcalf, Phys. Rev. A **35**, 1535 (1987).
[38] J. Fortágh and C. Zimmermann, Rev. Mod. Phys. **79**, 235 (2007).
[39] H. Müntinga, H. Ahlers, M. Krutzik, A. Wenzlawski, S. Arnold, D. Becker, K. Bongs, H. Dittus, H. Duncker et al., Phys. Rev. Lett. **110**, 093602 (2013).
[40] C. Deppner, W. Herr, M. Cornelius, P. Stromberger, T. Sternke, C. Grzeschik, A. Grote, J. Rudolph, S. Herrmann et al., Phys. Rev. Lett. **127**, 100401 (2021).
[41] M. D. Lachmann, H. Ahlers, D. Becker, A. N. Dinkelaker, J. Grosse, O. Hellmig, H. Müntinga, V. Schkolnik, S. T. Seidel et al., Nat. Commun. **12**, 1317 (2021).
[42] K. Frye, S. Abend, W. Bartosch, A. Bawamia, D. Becker, H. Blume, C. Braxmaier, S.-W. Chiow, M. A. Efremov et al., EPJ Quantum Technol. **8**(1), 1 (2021).
[43] J. Rudolph, W. Herr, C. Grzeschik, T. Sternke, A. Grote, M. Popp, D. Becker, H. Müntinga, H. Ahlers et al., New J. Phys. **17**, 065001 (2015).
[44] A. P. Kazantsev, G. I. Surdutovich, and V. P. Yakovlev, *Mechanical Action of Light on Atoms* (World Scientific Publishing Co. Pte. Ltd., Singapore, 1990).
[45] S. Marksteiner, R. Walser, P. Marte, and P. Zoller, Appl. Phys. B **60**, 145 (1995).
[46] R. Grimm, M. Weidemüller, and Y. B. Ovchinnikov, "Optical dipole traps for neutral atoms," in *Advances in Atomic, Molecular, and Optical Physics* (Elsevier, 2000), Vol. 42, pp. 95–170.
[47] P. W. Milonni and J. H. Eberly, *Laser Physics* (Wiley, Inc., Hoboken, NJ, 2010).
[48] K. Bongs, S. Burger, S. Dettmer, D. Hellweg, J. Arlt, W. Ertmer, and K. Sengstock, Phys. Rev. A **63**, 031602 (2001).

[49]S. Kanthak, M. Gebbe, M. Gersemann, S. Abend, E. M. Rasel, and M. Krutzik, New J. Phys. **23**, 093002 (2021).

[50]F. Dalfovo, S. Giorgini *et al.*, Rev. Mod. Phys. **71**, 463 (1999).

[51]G. Baym and C. J. Pethick, Phys. Rev. Lett. **76**, 6 (1996).

[52]J. Teske, M. R. Besbes, B. Okhrimenko, and R. Walser, Phys. Scr. **93**, 124004 (2018).

[53]W. Ketterle, D. S. Durfee, and D. M. Stamper-Kurn, "Making, probing and understanding Bose-Einstein condensates," arxiv:cond-mat/9904034 (1999).

[54]Y. Castin and R. Dum, Phys. Rev. Lett. **77**, 5315 (1996).

[55]Y. Kagan, E. L. Surkov, and G. V. Shlyapnikov, Phys. Rev. A **54**, R1753 (1996).

[56]M. Meister, S. Arnold, D. Moll, M. Eckart, E. Kajari, M. A. Efremov, R. Walser, and W. P. Schleich, "Efficient description of Bose–Einstein condensates in time-dependent rotating traps," in *Advances in Atomic, Molecular, and Optical Physics* (Elsevier, 2017), Vol. 66, pp. 375–438.

[57]A. L. Fetter and D. L. Feder, Phys. Rev. A **58**, 3185 (1998).

[58]D. Becker, M. D. Lachmann, S. T. Seidel, H. Ahlers, A. N. Dinkelaker, J. Grosse, O. Hellmig, H. Müntinga, V. Schkolnik *et al.,* Nature **562**, 391 (2018).

[59]D. C. Aveline, J. R. Williams, E. R. Elliott, C. Dutenhoffer, J. R. Kellogg, J. M. Kohel, N. E. Lay, K. Oudrhiri, R. F. Shotwell *et al.,* Nature **582**, 193 (2020).

[60]G. Gauthier, I. Lenton, N. M. Parry, M. Baker, M. J. Davis, H. Rubinsztein-Dunlop, and T. W. Neely, Optica **3**, 1136 (2016).

[61]C. A. Sackett and J. A. Stickney, Phys. Rev. A **107**, 063305 (2023).

[62]W. Herr, "*Eine kompakte Quelle quantenentarteter Gase hohen Flusses für die Atominterferometrie unter Schwerelosigkeit,*" Ph.D. thesis (Gottfried Wilhelm Leibniz Universität Hannover, 2013).

[63]J. D. Jackson, "Electrodynamics, classical," in *Digital Encyclopedia of Applied Physics* (Wiley-VCH Verlag GmbH & Co. KGaA, Weinheim, Germany, 2003).

[64]J. Nocedal and S. Wright, *Numerical Optimization, Springer Series in Operations Research and Financial Engineering* (Springer New York, 2006).

04 March 2024 12:38:33